Nanoscale Advances

ROYAL SOCIETY OF CHEMISTRY

PAPER

View Article Online
View Journal | View Issue

Cite this: *Nanoscale Adv.*, 2023, **5**, 2216

Synthesis of $Ti_3C_2T_x/MnO_2$ composites for synergistic catalytic/photothermal-based bacterial inhibition†

Ting Hu,[a] Zhilong Xu,[a] Peiying Zhang,[b] Lei Fan, *[a] Juqun Xi,*[b] Jie Han [a] and Rong Guo [a]

Human inflammation caused by bacterial infection threatens global public health. The abuse of antibiotics often leads to the development of drug resistance in bacteria. To address this issue, nanozymes with peroxidase-like (POD-like) activity have often been reported for bacteriostasis with the assistance of catalytic substrate hydrogen peroxide (H_2O_2). However, it is difficult to achieve efficient bactericidal outcomes only through exertion of the POD-like activity of nanozymes. Here, MnO_2 loaded $Ti_3C_2T_x$ ($Ti_3C_2T_x/MnO_2$) was prepared by a two-step reaction method, in which MnO_2 showed high oxidase-like (OXD-like) activity to elevate the levels of reactive oxygen species (ROS) without H_2O_2 and $Ti_3C_2T_x$ exhibited high photothermal conversion efficiency to induce hyperthermia. Thus, the obtained $Ti_3C_2T_x/MnO_2$ realized synergistic catalytic/photothermal-based bacterial inhibition, including for Gram-negative bacteria (*Escherichia coli*), Gram-positive bacteria (*Staphylococcus aureus*), and methicillin-resistant *Staphylococcus aureus*. Importantly, $Ti_3C_2T_x/MnO_2$ with near-infrared light irradiation successfully promoted *Staphylococcus aureus*-infected wound healing in mouse models, representing an alternative treatment to fight against bacterial infection.

Received 17th December 2022
Accepted 27th February 2023

DOI: 10.1039/d2na00923d

rsc.li/nanoscale-advances

Introduction

Diseases caused by bacterial infections are one of the major problems affecting human health worldwide.[1,2] The discovery of antibiotics has reduced the mortality rate of bacterial infections. However, bacteria have a short reproductive cycle and are prone to rapid mutation. Some of them are becoming resistant to antibiotics.[3,4] In addition, the abuse of antibiotics aggravates the development of drug resistance in bacteria.[5–8] The main solution to this problem is to constantly improve conventional antibiotic molecules to produce various new antibiotic derivatives, but it is still hard to meet the need for eliminating resistant bacteria.[9] Furthermore, some organic antibacterial agents, which have been used to solve the problem of bacterial resistance, also face problems in terms of biosafety and stability.[10–12] Therefore, there is an urgent need to develop new antibacterial strategies to address the problem of drug resistance in bacteria.

Nanozymes are a class of nanomaterials with enzyme-like catalytic activity.[13,14] The unique advantages of nanozymes as antibacterial agents include low cost, versatility, good stability, high catalytic activity, and easy penetration into biofilms.[15,16] To date, lots of different compositions and structures of nanozymes have been used in antibacterial research, including metal oxides,[17–20] metal sulfides,[17,19,21] noble metals,[4,22,23] and carbon-based nanozymes.[24–26] Among them, MnO_2 has attracted much attention due to its good biosafety, high catalytic activity and easy preparation. MnO_2, as a nanozyme with multi-enzyme-mimicking activities, can generate high-intensity ROS to cut off the nucleic acid, make the protein inactive, and degrade a variety of molecules in bacteria, thus exhibiting good potential for application in killing bacteria.[27,28] In terms of POD-like activity, the antibacterial capacity is based on the catalytic reaction between MnO_2 and H_2O_2. However, the deficiency of endogenous H_2O_2 and the instability of exogenous H_2O_2 make the POD-like activity-dependent antibacterial strategy fail easily. So, how to improve the antibacterial ability of MnO_2 is worth investigating. The OXD mimetic enzyme does not require the addition of H_2O_2 to produce ROS for bacterial inhibition. So, the construction of MnO_2 nanostructures with good OXD catalytic activity is very important. In addition, drug combination is a common clinical treatment protocol for anti-infection therapy. Inspired by this, we here try to integrate catalytic therapy and photothermal therapy.[29,30]

Currently, varieties of photothermal agents have been reported for bacterial inhibition, among which MXenes are an emerging class of two-dimensional layered materials with excellent photothermal properties.[31–34] Among the different

[a]*School of Chemistry and Chemical Engineering, Yangzhou University, Yangzhou 225002, P. R. China. E-mail: fanlei@yzu.edu.cn*

[b]*Department of Pharmacology, Institute of Translational Medicine, School of Medicine, Yangzhou University, Yangzhou 225002, China. E-mail: xijq@yzu.edu.cn*

† Electronic supplementary information (ESI) available. See DOI: https://doi.org/10.1039/d2na00923d

types of MXene materials, $Ti_3C_2T_x$ shows the best photothermal performance with 808 nm laser radiation.[35] However, it's difficult to obtain a good antibacterial effect with $Ti_3C_2T_x$ alone. In the absence of light, the sterilization efficiency decreased dramatically. So how to achieve long-term sterilization is a problem. Therefore, if $Ti_3C_2T_x$ could be combined with other materials, such as nanozymes, to achieve a synergistic effect of multiple functions, a good sterilization effect should be achieved.

Based on the above, we prepared $Ti_3C_2T_x/MnO_2$ composites with high OXD-like activity and photothermal conversion ability for efficient bacterial inhibition. The MnO_2 in $Ti_3C_2T_x/MnO_2$ is capable of exerting a variety of mimetic enzyme properties. Specifically, their high OXD-like activity can be utilized directly for bacterial inhibition without the addition of H_2O_2.[36–38] At the same time, the excellent photothermal conversion efficiency of $Ti_3C_2T_x$ can greatly improve the sterilization efficiency. Therefore, we could establish a catalytic-photothermal synergistic antibacterial system using nanozymes and $Ti_3C_2T_x$ to develop highly and enduringly efficient antibacterial agents.

Experimental section

Materials

MAX (Ti_3AlC_2) was purchased from 11 Technology (Jilin, China). Lithium fluoride (LiF), hydrochloric acid (HCl), hydrogen peroxide (H_2O_2), and potassium permanganate ($KMnO_4$) were purchased from Sinopharm Chemical Reagent (Shanghai, China). Dopamine hydrochloride (DA·HCl) and Tris buffered saline (TBS) were purchased from Shanghai Maclean's Biochemical Technology Co., Ltd (Maclean's reagent), and 3,3′,5,5′-tetramethylbenzidine (TMB) was purchased from Sigma-Aldrich (USA). All reagents were used as received.

Preparation of $Ti_3C_2T_x$

First, 1 g of LiF and 20 mL of 9 M HCl were added into a Teflon beaker and stirred at 400 rpm for 1 h. Then 1 g of MAX (Ti_3AlC_2) was added slowly while the temperature was set to 35 °C and stirred for 48 h. After this, the reaction solution was centrifuged (3500 rpm, 10 min) and washed with water until the pH was about 5, and then freeze-dried to obtain the MXene ($Ti_3C_2T_x$ (S0)). The reactions were all performed in a fume hood.

Preparation of $Ti_3C_2T_x$@PDA

The obtained $Ti_3C_2T_x$ was prepared as a 100 mL 5 mg mL^{-1} dispersion and 0.25 g of dopamine hydrochloride was added and stirred at room temperature for 1 h. Then 25 mL of Tris buffer was added and stirred for 24 h. The powder was washed several times with ultrapure water and dried at 60 °C for 48 h under vacuum to obtain $Ti_3C_2T_x$@PDA.

Preparation of $Ti_3C_2T_x/MnO_2$

The $Ti_3C_2T_x$@PDA powder was prepared as a 3 mg mL^{-1} solution, and then 10 mL of 0.02 M $KMnO_4$ solution was added into the solution. The solution was kept in an oil bath at 70 °C for 3 h. The solution was then cooled to room temperature and washed with ultrapure water and anhydrous ethanol and dried under vacuum at 40 °C for 12 h. $Ti_3C_2T_x/MnO_2$ (S2) powders with a mass ratio of $Ti_3C_2T_x$@PDA to $KMnO_4$ of 1 : 1 was obtained. Furthermore, for comparison by changing the mass ratio of $Ti_3C_2T_x$@PDA to $KMnO_4$ to 1 : 0.5 and 1 : 2, different $Ti_3C_2T_x/MnO_2$ powders were prepared and named S1 and S3.

Bacterial culture and antibacterial experiments *in vitro*

Escherichia coli (*E. coli*), *Staphylococcus aureus* (*S. aureus*), and methicillin-resistant *Staphylococcus aureus* (MRSA) were selected to study the antibacterial properties. Luria–Bertani medium (LB medium) was prepared in advance. 4 g NaCl, 2 g yeast powder, and 4 g tryptone were weighed to make a 400 mL solution, and then it was sterilized by autoclaving for 15 minutes. For the solid medium, 2% agar was added. After autoclaving, it was used on an ultra-clean workbench in time to make culture plates. After solidification and drying, these plates were placed in a 4 °C refrigerator for storage. Before the experiment, the workbench was sterilized by UV light irradiation for 30 min. According to the planned time, the bacterial liquid was inoculated in advance, then transferred according to a ratio of 1 : 100, and continued to be incubated at a constant temperature at 37 °C in a shaker for about 3 hours. After this, the $OD_{600\ nm}$ values of the bacterial solution were detected using an ultraviolet spectrophotometer, and the solution was taken out for use when the $OD_{600\ nm}$ value was between 0.7 and 0.8. A 1 mL reaction system was constructed by adding 100 μL of the material solution and 100 μL of the bacterial solution to 800 μL of sterile sodium acetate solution at pH = 4.5. Homogeneous mixing was performed using a pipette gun. The inhibition incubation time was 30 minutes for each group: (I) control; (II) S0; (III) S0 + laser; (IV) S2; (V) S2 + laser. Finally, for the bacterial action, the bacterial solution was spread evenly on LB solid medium plates with sterile glass balls and incubated upside down in a 37 °C incubator at a constant temperature. The number of colonies in each group will be counted the next day to evaluate the antibacterial ability of the material.

Skin wound treatment

Animal experiments were carried out following the Guidelines for Care and Use of Laboratory Animals of Yangzhou University and approved by the Animal Ethics Committee of Medical College of Yangzhou University (YXYLL-2022-44). Selected male BALB/c mice (5–6 weeks, ~22 g) were randomly divided into five groups (6 mice in each group; $n = 6$): (I) control group; (II) S0; (III) S0 + laser; (IV) S2; (V) S2 + laser. Then a 7–8 mm diameter circular wound was cut out on the back of each mouse and 20 μL of *S. aureus* bacteriological solution with an $OD_{600\ nm}$ value of about 0.8 was added dropwise. 20 μL of bacteriological solution was added dropwise again on the bandaged sterile gauze to establish a wound model. Twenty-four hours after infection, the wounds of mice in groups I–V were treated with 30 μL of sterile sodium acetate solution with pH = 4.5, 30 μL of 250 μg mL^{-1} S0, and 30 μL of 250 μg mL^{-1} S2, respectively. Mice were weighed, and wounds were photographed daily. On day 12, all mice were sacrificed. Wound tissues and major organs were fixed in 4%

formaldehyde solution for histopathological analysis by hematoxylin–Eosin (H&E) staining.

Results and discussion

Characterization of $Ti_3C_2T_x/MnO_2$

In order to synthesize the $Ti_3C_2T_x/MnO_2$ composites a two-step synthesis process was used. First, the etched $Ti_3C_2T_x$ was added into dopamine hydrochloride to form a layer of polydopamine (PDA) on its surface. Secondly, $KMnO_4$ was added to synthesize $Ti_3C_2T_x/MnO_2$ using the redox reaction between PDA and $KMnO_4$, as shown in Scheme 1.

Detailed characterization studies of $Ti_3C_2T_x$@PDA and $Ti_3C_2T_x/MnO_2$ were carried out to investigate the surface morphology and composition. The presence of N elements in addition to Ti and C elements as shown in Fig. S1a† is evidence of PDA loading on the $Ti_3C_2T_x$ surface. The zeta potential (Fig. S1b†) of $Ti_3C_2T_x$ was negatively charged (−31.27 mV). After loading of PDA, the zeta potential was increased to −25.57 mV.[39] From transmission electron microscopy (TEM) and scanning electron microscopy (SEM) patterns shown in Fig. S2,† it was seen that the formation of PDA on the surface did not change the morphology of $Ti_3C_2T_x$, which remained as a layered structure. After the addition of $KMnO_4$, $Ti_3C_2T_x/MnO_2$ was obtained. The SEM and TEM patterns demonstrate that the morphology of the sample as shown in Fig. 1a and b is homogeneous. And the flakes of MnO_2 grew on the surface of $Ti_3C_2T_x$. In contrast, the S1 and S3 samples were not so inhomogeneous as shown in Fig. S2 and S3.† The S1 sample is shown as bare $Ti_3C_2T_x$, where no flakes were found on its surface; while the S3 sample has excessive MnO_2 flakes. As shown in Fig. 1c, the 0.420 and 0.276 nm lattice distances in the HRTEM image could correspond to the (101) and (301) crystal planes of MnO_2, respectively, proving that the product is MnO_2.

In order to investigate the crystal structure of the materials, S0 and S2 were characterized by X-ray diffraction (XRD) (Fig. 1d). In the XRD pattern of the S0 sample, the disappeared peak located at 39° in the XRD spectrum of Ti_3AlC_2 (JCPDS No. 52-0875) proves the successful etching of $Ti_3C_2T_x$.[40] The S2 sample has no obvious broad peak. And Ti, C, Mn, and O elements are uniformly distributed (Fig. 1e–i). This further proves the formation of MnO_2. In addition, the disappearance of the N element also indicates that the PDA supported on the $Ti_3C_2T_x$ surface had been completely consumed. To further determine the composition of this material, the sample was determined by X-ray photoelectron spectroscopy (XPS) analysis (Fig. 1j–m). From the full spectrum, it can be found that the material contains the elements Ti, C, O, and Mn. The N element was eliminated during the synthesis of MnO_2 (disappearance of the N peak), and the element contents shown in Table S1† further concluded that PDA was completely consumed. The O 1s spectrum of S2 can be split into three characteristic peaks. The low-binding energy O peak (blue line) at 531.5 eV corresponds to Mn–OH bonds, and the high-binding energy O peak (red line) at 530.2 eV could be assigned to Mn–O–Mn. The H–O–H peak at 532.7 eV appeared from adsorbed water molecules. The loading of MnO_2 nanosheets on $Ti_3C_2T_x$ provided active centers and reaction sites to improve the catalytic performance. The Mn 2p spectrum with a separation spin energy of 11.7 eV (as shown in Fig. 1l), where Mn $2p_{3/2}$ and Mn $2p_{1/2}$ are located at 642.4 and 654.1 eV, confirms the formation of MnO_2.[41,42] This could also be proved by the separation spin energy of 4.8 eV of two characteristic peaks at 84.3 and 89.1 eV in the spectrum of Mn 3s shown in Fig. 1m. Furthermore, the binding energies of 282.2, 284.8, 286.3, and 288.5 eV can be attributed to C–Ti, C–C, C–O, and C=O bonds based on the high-resolution spectra of C 1s. In the Ti 2p spectra (Fig. S4a and b†), the $2p_{3/2}$ and $2p_{1/2}$ peaks of Ti^{3+} appeared at 458.8 and 464.6 eV. In addition to this, Ti–C with $2p_{3/2}$ and $2p_{1/2}$ peaks appeared at 456 and 461.3 eV, respectively, indicating that the composite retains the structure of $Ti_3C_2T_x$.[43] The specific surface areas of the four materials analyzed by nitrogen adsorption and desorption (Fig. S4c†) were 10.02, 27.52, 112.53, and 102.38 $m^2 g^{-1}$, respectively (Table S2†). The S2 sample has the largest specific surface area, which indicates that the material has more active sites susceptible to catalysis.

Enzyme-like catalytic activity of $Ti_3C_2T_x/MnO_2$

According to previous reports,[44–46] MnO_2 exhibits OXD-like activity. So, the enzyme-like activity of the synthesized $Ti_3C_2T_x$/

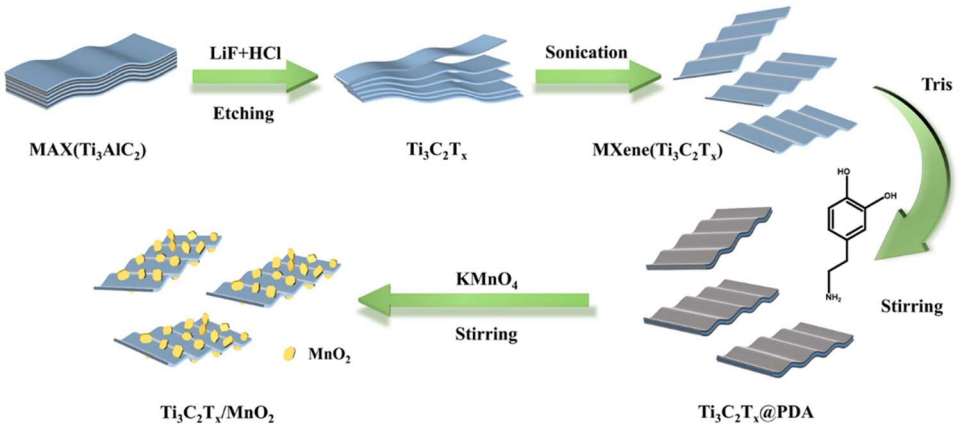

Scheme 1 Schematic diagram of the preparation of $Ti_3C_2T_x/MnO_2$ composites.

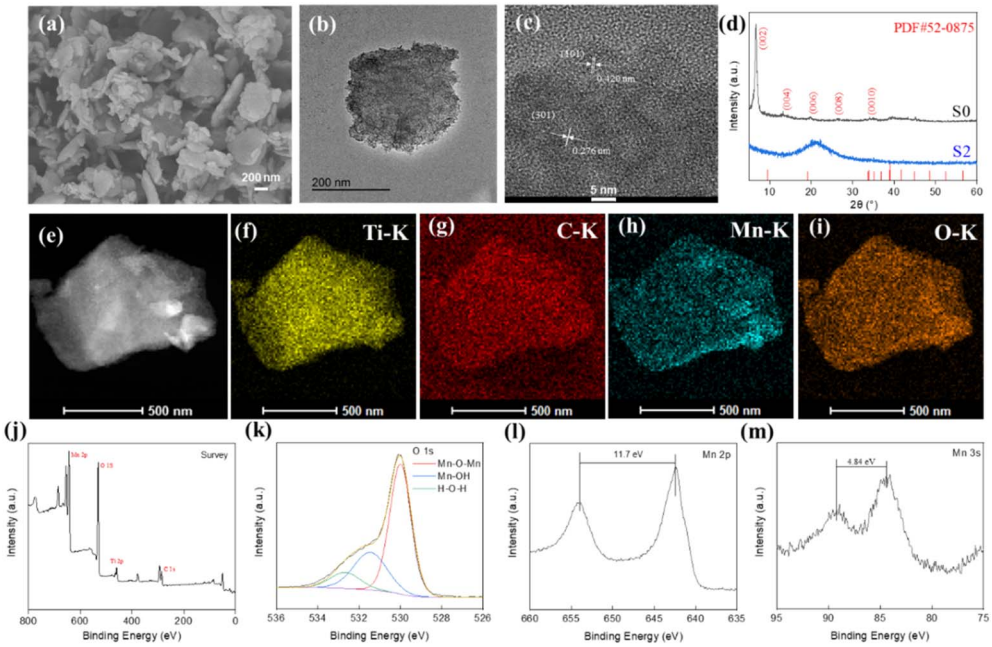

Fig. 1 S2 sample: (a) SEM image; (b) TEM image; (c) HRTEM image; (d) XRD patterns for both S0 and S2; (e) STEM image; (f–i) Ti, C, Mn and O elemental mapping images; (j–m) XPS spectra of the full spectrum, O 1s, Mn 2p and Mn 3s regions.

MnO_2 composites was investigated. The OXD-like activities of $Ti_3C_2T_x/MnO_2$ synthesized according to the different ratios were also compared. There is a clear characteristic absorption peak at 652 nm as shown in Fig. 2a accompanied by a color change to blue in the presence of O_2. S1 exhibits relatively low OXD-like activity at 652 nm. The catalytic activity of S3 is significantly increased compared to S1, while S2 has the highest absorbance at 652 nm, confirming its highest catalytic activity. The variation of absorbance with time for the different nanozymes (Fig. S5a†) also demonstrates the excellent enzyme mimicking activity of S2. Similar to the other oxidase mimics,[47,48] the catalytic activity of $Ti_3C_2T_x/MnO_2$ was dependent on pH and the substrate concentration (Fig. 2b and S5c†). In particular, the optimum pH was 4.5. Michaelis–Menten curves were obtained for the above

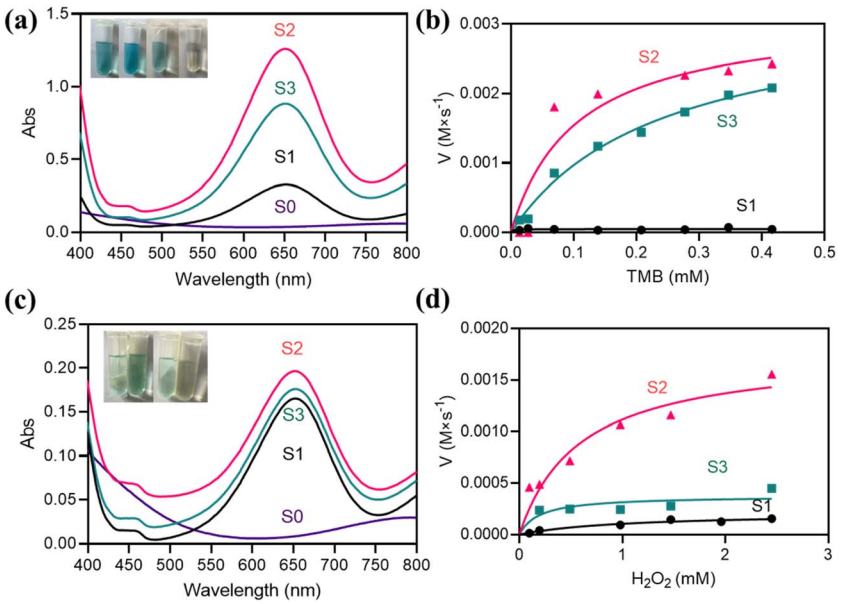

Fig. 2 (a) UV absorption spectra of TMB + S0, TMB + S1, TMB + S2 and TMB + S3; (b) concentration *versus* the reaction rate for TMB as a substrate; (c) UV absorption spectra of TMB + H_2O_2 + S0, TMB + H_2O_2 + S1, TMB + H_2O_2 + S2 and TMB + H_2O_2 + S3; (d) concentration *versus* the reaction rate for H_2O_2 as a substrate.

three nanozymes over a range of concentrations of TMB, and the kinetic parameters (K_m and V_{max}) are summarized in Table S3.† By comparing V_{max}/K_m at different ratios, it was found that the V_{max}/K_m of S2 is the largest, indicating the highest catalytic activity. Furthermore, the maximum specific surface area of S2 as shown in Fig. S3c† further supports this result.

In addition to OXD-like activity, the prepared material also exhibits valid POD-like enzyme mimetic activity. The POD-like activity was assessed by catalytic TMB oxidation in the presence of H_2O_2 as a model reaction with a characteristic absorption peak at 652 nm accompanied by a change in colour to blue. As shown in Fig. 2c, the characteristic absorption peak at 652 nm indicates that the composite has significant POD-like activity. Similar to the OXD-like activity, S2 had better POD-like activity (Fig. S5b and d†). The Michaelis–Menten curves for S1, S2, and S3 are shown in Fig. 2d. In Table S4,† the V_{max}/K_m values of the S2 sample are higher than those of other samples, which also indicates that S2 has higher peroxidase-like activity. In addition, pure $Ti_3C_2T_x$ did not show any OXD-like activity and POD-like activity at 652 nm, thus demonstrating that the catalytic activity was mainly provided by MnO_2.

Photothermal properties of $Ti_3C_2T_x/MnO_2$

The inhibition of bacteria by catalytic production of ROS alone is often not satisfactory, so photothermy is introduced here to achieve synergistic antibacterial activity. The related literature has reported that $Ti_3C_2T_x$ has good photothermal properties.[49–51] Therefore, the photothermal conversion properties of the composites were investigated. The $Ti_3C_2T_x/MnO_2$ samples were irradiated using an 808 nm NIR laser with a power density of 2.0 W cm^{-2}, and the photothermal conversion performance, as well as the stability performance were studied (Fig. 3). Fig. 3a shows the temperature rise curves for H_2O, 250 μg mL^{-1} of S0, S1, S2, and S3 solutions. The temperatures of the sample solutions increased by 0.7 °C, 23.2 °C, 22.6 °C, 24.6 °C, and 20.7 °C, respectively. After 10 min of NIR light irradiation, S2 showed better photothermal conversion performance than other materials. It has been reported that as MnO_2 increases, the temperature of the system increases as well.[52,53] The small difference between the increasing temperatures of S0 and S1 indicates that loading a certain amount of MnO_2 on the $Ti_3C_2T_x$ surface is more conducive to the improvement of photothermal conversion properties. However, there is a slight decrease in the temperature rise of S3, which is due to the excessive amount of MnO_2, making it difficult for $Ti_3C_2T_x$ to exert the effect of photothermal conversion. The optimum conditions for the concentration of the materials were explored (Fig. 3b). When the concentration was 50 and 150 μg mL^{-1}, the temperature increased by 5.3 °C and 12.8 °C, respectively. In contrast, at a concentration of 250 μg mL^{-1}, the temperature was able to increase by 24.6 °C. When the concentration was increased to 300 μg mL^{-1}, the temperature rise did not increase too much, so a concentration of 250 μg mL^{-1} was chosen as the study concentration. And the investigation of power effects as shown in Fig. 3c yielded an optimum power of 2.0 W cm^{-2}. In addition, at the same concentration, the stability performance of S2 solution was studied as shown in Fig. 3d. After three on/off irradiations, the S2 solution still maintained high photothermal conversion abilities. The photothermal conversion efficiency was measured by Roper's method. The relevant calculations were obtained as shown in Fig. 3e and f. The photothermal conversion efficiency (η) was 65.97%. The above results further demonstrate that S2 can efficiently and rapidly convert light to heat, and this property can be used in antibacterial applications.

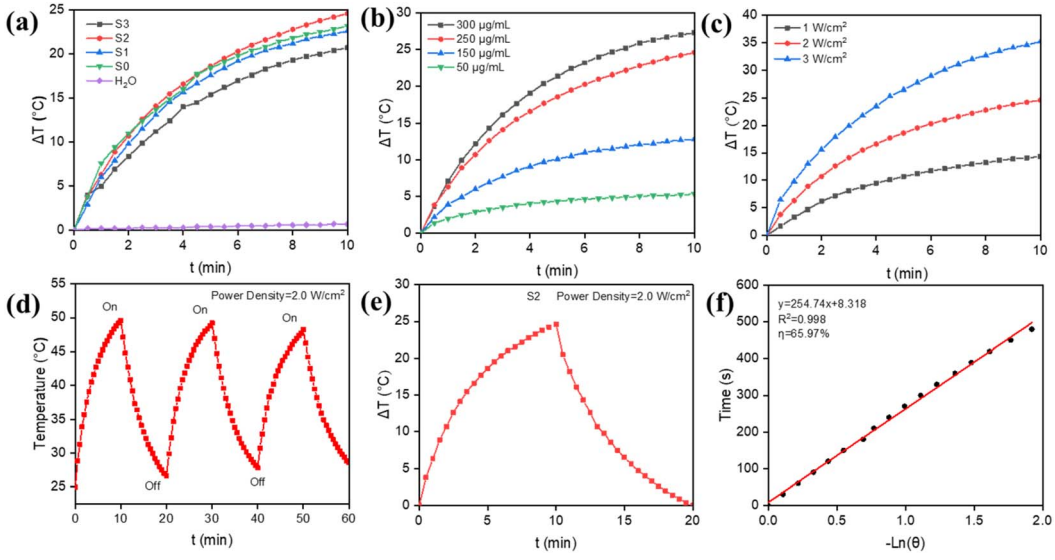

Fig. 3 (a) Temperature rise curves for H_2O, S0 and different ratios of $Ti_3C_2T_x/MnO_2$ under NIR light (808 nm, 2 W cm^{-2}) irradiation; (b) temperature rise profiles of different concentrations of S2 solution under NIR light (808 nm, 2 W cm^{-2}) irradiation; (c) temperature rise profiles of different powers of NIR light irradiation for S2; (d) stability performance of S2 under NIR light irradiation in the cycling stability performance graph; (e) temperature change of the solution after 600 s of photothermal action of S2 under 808 nm NIR light irradiation followed by 600 s of NIR light switch-off; (f) negative natural logarithm ($-\ln\theta$) of the cooling time curve of S2 after 600 s; the sample concentration was 250 μg mL^{-1}.

Antibacterial conditions of $Ti_3C_2T_x/MnO_2$ *in vitro*

Most of the current studies use POD-like enzymes in coordination with H_2O_2 to achieve bacterial inhibition, but this study focuses on the activity of OXD-like nanozymes, which can effectively convert O_2 to ROS without addition of H_2O_2 to avoid damage to normal cells. According to the reported results,[54] it has been shown that the bacteria can also be inhibited by the photothermal conversion capability of $Ti_3C_2T_x$. Therefore, a catalytic-photothermal synergistic bacterial inhibition system was constructed. Herein, 808 nm irradiation was chosen to assess the inhibition performance of S2 using a plate counting method. First, the inhibition of S0, S1, S2, and S3 under acidic conditions was investigated *in vitro*. By comparing the bacterial survival of Gram-positive (*E. coli*) and Gram-negative (*S. aureus*) bacteria (Fig. 4), we concluded that S2 was the most effective in inhibiting bacteria. Next, the effect of the concentration and incubation time of the material on the inhibition of *E. coli* was studied. As can be seen in Fig. S6a and b,† the viability of the bacteria gradually decreased as the concentration of the material and the incubation time increased, indicating that the inhibition effect of S2 was concentration and time-dependent. In summary, we chose a concentration of 250 μg mL^{-1} and an incubation time of 30 minutes as the study conditions. As shown in Fig. S6c and d,† the inhibition effect of S2 on *E. coli* was related to the power and irradiation time of the NIR laser. As can be seen from Fig. S6c† the survival rate of *E. coli* decreased gradually with the increase of laser power, and the bacterial viability decreased significantly at 2.0 W cm^{-2}. And when the power increased to 3.0 W cm^{-2}, the decrease in bacterial viability was not significant. As shown in Fig. S6d,† the survival rate of *E. coli* gradually decreased when the light exposure was extended. The bacterial viability of *E. coli* decreased significantly when the light time reached 8 minutes, which is better than lighting for 6 minutes. If the light time was extended for 10 minutes, the effect was not significantly improved. Therefore, good photothermal conversion performance can achieve a certain antibacterial effect, but photothermal therapy is affected by its power and irradiation time. Low light power and short-duration lighting do not achieve a good antibacterial effect. So, in order to avoid too high a power or too long a light time leading to healthy tissue damage, a NIR laser irradiation power of 2.0 W cm^{-2} and an irradiation time of 8 minutes were chosen for the following experiments. Similarly, the analysis in Fig. S6e–h† shows that for *S. aureus*, a concentration of 250 μg mL^{-1}, an incubation time of 30 minutes, a NIR laser power of 2.0 W cm^{-2}, and an irradiation time of 10 minutes were used to achieve high bacterial inhibition.

Detection of bacterial ROS induced by $Ti_3C_2T_x/MnO_2$

Based on the fact that the antibacterial mechanism of the mimetic enzyme with OXD-like activity is attributed to the ROS generated during the catalytic reaction, we examined the ROS levels in S0 and S2. The ROS levels of the bacteria in the different treatment groups were subsequently measured using DCFH. The fluorescence intensity shown in Fig. 5 reflects the level of ROS in the bacterial system. In the case of *S. aureus*, the fluorescence intensity of the S2-treated group was increased compared with that of the control and S0-treated groups. Similar results were obtained for *E. coli* and MRSA. Therefore, ROS production in the system *via* catalytic production of mimetic OXD activity is a factor contributing to bacterial mortality.

Antibacterial effect of $Ti_3C_2T_x/MnO_2$ with and without NIR light

The irradiation effect on bacterial inhibition of S2 for *E. coli*, *S. aureus*, and MRSA was also studied. As can be seen in Fig. 6a, S0 and S2 showed a slight reduction in bacterial viability (<−0.63 lg) because S2 had OXD-like activity to produce ROS to inhibit bacterial viability. The bacterial inhibition effect was significantly enhanced by the involvement of NIR. When *E. coli* was treated with S0 + laser for 8 minutes, the bacteria decreased by −1.62 lg. The antibacterial efficiency of S2 + laser was decreased significantly by −3.82 lg. The photographs of the bacteria colonies shown in Fig. 6a clearly showed that S2 + laser had the optimal antibacterial effect. On the one hand, the improvement in antibacterial performance is due to the synergistic effect of photothermy and nanozyme catalysis. On the other hand, the photothermal effect will also improve the performance of nanozyme catalysis and further kill bacteria.[55,56] *S. aureus* (Fig. 6b) was reduced by −0.77 lg and −1.93 lg for S0 and S2 without the laser, and the bacteria were significantly reduced by

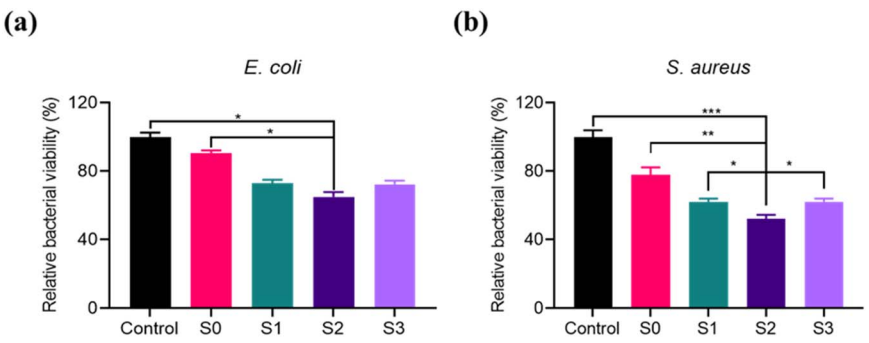

Fig. 4 (a and b) Bacterial survival of *E. coli* and *S. aureus* after incubation with S0, S1, S2 and S3 under acidic conditions; the concentration was 250 μg mL^{-1}; the reaction time was 30 minutes. *p < 0.05, **p < 0.01, and ***p < 0.001.

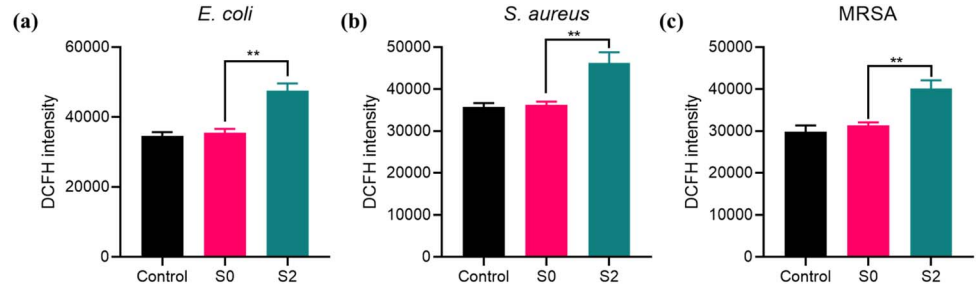

Fig. 5 The fluorescence signal of *E. coli* (a), *S. aureus* (b) and MRSA (c) after treatment with S0 and S2; $^{**}p < 0.01$.

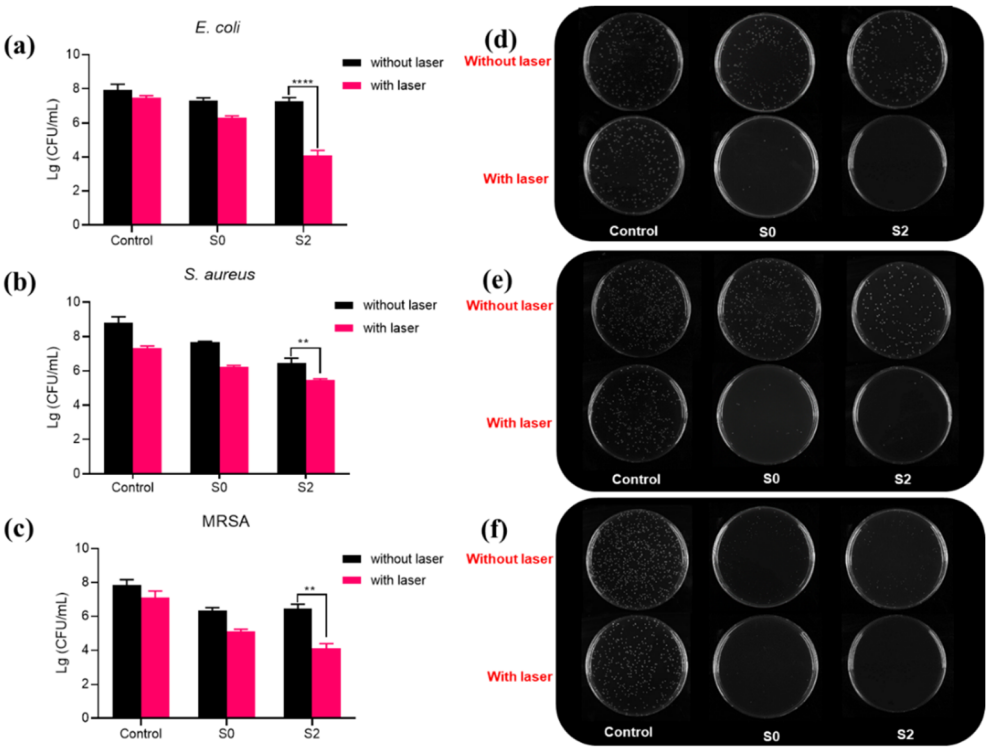

Fig. 6 (a–c) Survival of bacteria after incubation with S0 and S2 with and without NIR light (808 nm; 2 W cm^{-2}) for *E. coli* (8 min), *S. aureus* and MRSA (10 min); (d–f) photographs of bacterial colonies; incubation time was 30 min; the sample concentration was 250 μg mL^{-1}; $^{**}p < 0.01$, and $^{****}p < 0.0001$.

−3.36 lg with the laser for S2. It is important to note that drug-resistant bacteria are usually more difficult to kill in bacterial infections. In contrast, the material in this paper is equally effective against MRSA. As can be seen in Fig. 6c, S2 + laser inhibited the viability of MRSA effectively and −3.75 lg reduction was observed. The efficient bactericidal effect of S2 + laser is further illustrated by the photographs of the colonies in Fig. 6d–f. These results suggest that S2-based catalytic-photothermal synergistic therapies have a broader spectrum of bactericidal activity than monotherapies (single photothermal therapy or ROS therapy).

Wound healing by $Ti_3C_2T_x/MnO_2$ *in vivo*

Their antibacterial properties in skin wound healing were assessed given their significant inhibition of bacteria *in vitro*. The S2 sample with the highest OXD-like activity was selected from the three samples as well as the carrier $Ti_3C_2T_x$ as a control for the treatment of wound healing in infected mouse skin. First, an approximately 8 mm diameter circular wound was created on the back of each mouse. Then the wounds were infected with *S. aureus* for 24 h to establish the mouse infection model, and the mouse wounds were treated with S0, S2, S0 + laser, and S2 + laser, respectively. During the 12 days of treatment, we recorded the photographs of the wounds, the wound size, and the weight of each mouse. As shown in Fig. 7a, the wounds of the S2 + laser group had scarred first, and the inflammation had subsided. Moreover, the bacterial count from the wound on day 3 (shown in Fig. 7b) indicated that the S2 + laser could heal the wound effectively. The count of *S. aureus* at the wound site is shown in Fig. 7b. On day 4, the scars in the S2

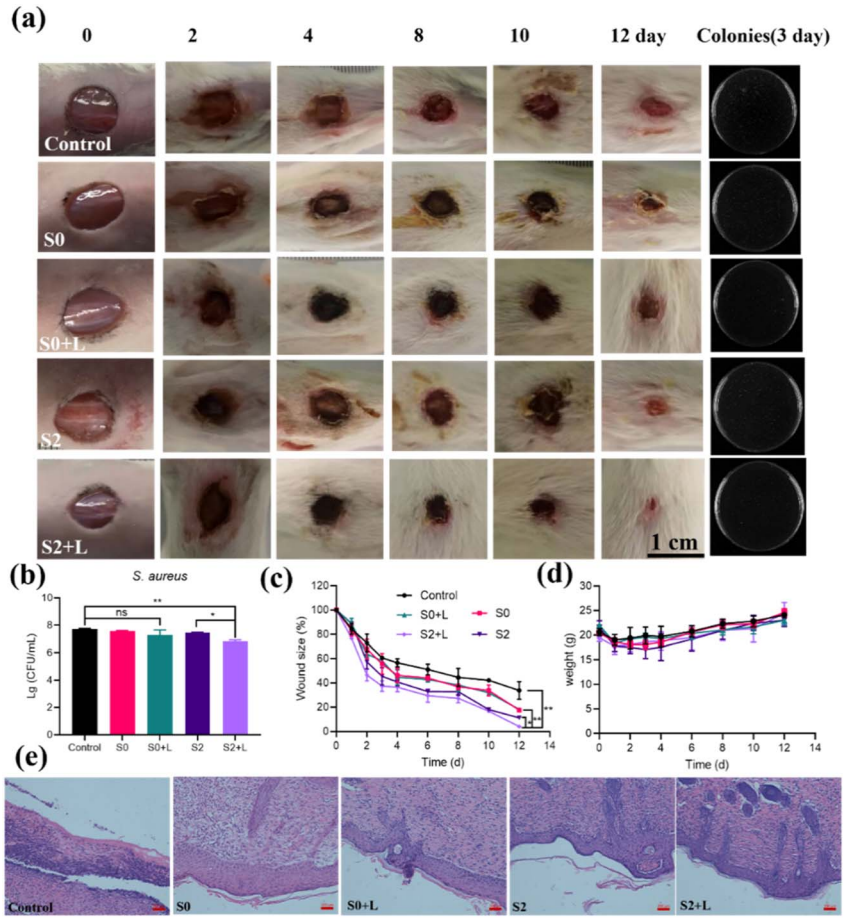

Fig. 7 The healing effect of different materials on infected wounds in mice: (a) photographs of the time of wounding in different groups; scale bar = 1 cm. Photos on the right are the corresponding agar plates of different groups of *S. aureus* isolated from the wound site on day 3; (b) number of bacteria surviving at the wound site on day 3; (c) change in wound size during wound healing in each group of mice; (d) change in body weight during wound healing in each group of mice; (e) H&E staining of wounds in each group of mice; scale bar is 200 μm. $*p < 0.05$, and $**p < 0.01$.

+ laser group were significantly smaller compared with those in the other groups. And the S2 + laser showed mostly intact epidermal structures on day 12. Analysis of the wound area as shown in Fig. 7c showed that S2 was effective in reducing infectious inflammation, mainly due to the OXD-like activity of S2. Wound healing was further accelerated under photothermal action. In comparison, the control, S0, S0 + laser and S2 groups showed wound closure rates of approximately 57%, 52%, 45% and 41% respectively (Fig. 7c). In addition, there was a significant upward trend in the body weight of the mice as the treatment effect improved (Fig. 7d), reflecting the good *in vivo* biocompatibility of S0 and S2. Hematoxylin–Eosin (H&E) staining was used to observe the wound tissue (Fig. 7e). In comparison with the control group, a large number of fibroblasts could be observed in the treated group, which presumes that the infected wound was recovering. The above results indicate that S2 showed optimal wound healing with the synergistic effect of NIR light.

To further illustrate the good wound healing effect of S2, all mice were sacrificed on day 12. The organs were paraffin-embedded, sectioned, and analyzed histopathologically for H&E staining of the major organs. As shown in the H&E-stained images of the heart, liver, spleen, lungs and kidneys, no significant damage was observed in the major organs. This indicates that S0 and S2 were not significantly toxic (Fig. S7a†). In addition, the survival of L02 cells after incubation with S0 and S2 nanoparticles was determined by the Cell Counting Kit-8 (CCK-8) colorimetric assay as shown in Fig. S7b,† also demonstrating the good *in vivo* compatibility of these two materials. In summary, S2 was effective in fighting bacterial infections and promoting wound healing, because S2 acts as a novel bacteriostatic agent by exerting its excellent OXD-like activity and photothermal properties.

Conclusion

In summary, we have synthesized a $Ti_3C_2T_x/MnO_2$ composite, which is capable of acting as an effective biocatalyst for the elimination of bacterial infections. Its unique advantage lies in the high oxidase-like activity and photothermal conversion properties of the composite. On the one hand, $Ti_3C_2T_x/MnO_2$ exerts OXD-like activity under weak acid conditions. This

property effectively kills *S. aureus* and MRSA. On the other hand, $Ti_3C_2T_x$ in $Ti_3C_2T_x/MnO_2$ has excellent photothermal properties, and the composite is able to achieve more efficient bacterial inhibition. Thus, our study provides evidence that the synergistic effect of multi-enzyme activity and photothermal properties of $Ti_3C_2T_x/MnO_2$ can make it a highly efficient bacterial inhibitor. This work offers the possibility of avoiding the misuse of antibiotics in clinical applications and ultimately improving the therapeutic efficacy of inflammatory conditions.

Conflicts of interest

There are no conflicts to declare.

Acknowledgements

This work was supported by the National Natural Science Foundation of China (No. 22072131) and the Priority Academic Program Development of Jiangsu Higher Education Institutions. We would also like to acknowledge the technical support received from the testing center of Yangzhou University.

References

1 S. M. Lehar, T. Pillow, M. Xu, L. Staben, K. K. Kajihara, R. V. Andlen, L. DePalatis, H. Raab, W. L. Hazenbos, J. H. Morisaki, J. Kim, S. Park, M. Darwish, B. C. Lee, H. Hernandez, K. M. Loyet, P. Lupardus, R. N. Fong, D. H. Yan, C. C. Halouni, E. Luis, Y. Khalfin, E. Plise, J. C. Heong, J. P. Lyssikatos, M. Strandh, K. Koefoed, P. S. Andersen, J. A. Flygare, M. W. Tan, E. J. Brown and S. M. Ariathasan, *Nature*, 2015, **527**, 323–328.
2 Z. Z. Wang, K. Dong, Z. Liu, Y. Zhang, Z. W. Chen, H. J. Sun, J. S. Ren and X. G. Qu, *Biomaterials*, 2017, **113**, 145–157.
3 P. Courvalin, *J. Intern. Med.*, 2008, **264**, 4–16.
4 Y. Zhang, P. Sun, L. Zhang, Z. Wang, F. Wang, K. Dong, Z. Liu, J. Ren and X. Qu, *Adv. Funct. Mater.*, 2019, **29**, 1808594.
5 S. B. Levy and B. Marshall, *Nat. Med.*, 2004, **10**, S122–S129.
6 M. J. Hajipour, K. M. Fromm, A. A. Ashkarran, D. J. de Aberasturi, I. R. de Larramendi, T. Rojo, V. Serpooshan, W. J. Parak and M. Mahmoudi, *Trends Biotechnol.*, 2012, **30**, 499–511.
7 D. Pornpattananangkul, L. Zhang, S. Olson, S. Aryal, M. Obonyo, K. Vecchio, C. M. Huang and L. F. Zhang, *J. Am. Chem. Soc.*, 2011, **133**, 4132–4139.
8 Y. Liang, Y. Liang, H. Zhang and B. Guo, *Asian J. Pharm. Sci.*, 2022, **17**, 353–384.
9 C. Willyard, *Nature*, 2017, **543**, 15.
10 K. Browne, S. Chakraborty, R. Chen, M. D. P. Willcox, D. S. Black, W. R. Walsh and N. Kumar, *Int. J. Mol. Sci.*, 2020, **21**, 7047.
11 S. Buffet-Bataillon, P. Tattevin, M. Bonnaure-Mallet and A. Jolivet-Gougeon, *Int. J. Antimicrob. Agents*, 2012, **39**, 381–389.
12 S. Chernousova and M. Epple, *Angew. Chem., Int. Ed.*, 2013, **52**, 1636–1653.
13 H. Wei and E. K. Wang, *Chem. Soc. Rev.*, 2013, **42**, 6060–6093.
14 S. Xu, L. Chang, Y. Hu, X. Zhao, S. Huang, Z. Chen, X. Ren and X. Mei, *J. Nanobiotechnol.*, 2022, **20**, 192.
15 G. Zhou, Q.-S. Shi, X.-M. Huang and X.-B. Xie, *Int. J. Mol. Sci.*, 2015, **16**, 21711–21733.
16 A. Gupta, R. Das, G. Y. Tonga, T. Mizuhara and V. M. Rotello, *ACS Nano*, 2018, **12**, 89–94.
17 S. Shi, S. Wu, Y. Shen, S. Zhang, Y. Xiao, X. He, J. Gong, Y. Farnell, Y. Tang, Y. Huang and L. Gao, *Theranostics*, 2018, **8**, 6149–6162.
18 L. Gao, K. M. Giglio, J. L. Nelson, H. Sondermann and A. J. Travis, *Nanoscale*, 2014, **6**, 2588–2593.
19 L. Gao, K. Fan and X. Yan, *Theranostics*, 2017, **7**, 3207–3227.
20 Z. Chen, J.-J. Yin, Y.-T. Zhou, Y. Zhang, L. Song, M. Song, S. Hu and N. Gu, *ACS Nano*, 2012, **6**, 4001–4012.
21 Y. Zhao, Q. Cai, W. Qi, Y. Jia, T. Xiong, Z. Fan, S. Liu, J. Yang, N. Li and B. Chang, *ChemistrySelect*, 2018, **3**, 9510–9516.
22 J. Y. Liu, D. A. Sonshine, S. Shervani and R. H. Hurt, *ACS Nano*, 2010, **4**, 6903–6913.
23 F. Kuang, Y. Chen, W. Shan, Y. Li, X. Bao, X. Gao, D. An and M. Qiu, *J. Mater. Chem. B*, 2022, **10**, 5582–5593.
24 B. Xu, H. Wang, W. Wang, L. Gao, S. Li, X. Pan, H. Wang, H. Yang, X. Meng, Q. Wu, L. Zheng, S. Chen, X. Shi, K. Fan, X. Yan and H. Liu, *Angew. Chem., Int. Ed.*, 2019, **58**, 4911–4916.
25 S. Liu, T. H. Zeng, M. Hofmann, E. Burcombe, J. Wei, R. Jiang, J. Kong and Y. Chen, *ACS Nano*, 2011, **5**, 6971–6980.
26 X. Liu, Z. Yan, Y. Zhang, Z. Liu, Y. Sun, J. Ren and X. Qu, *ACS Nano*, 2019, **13**, 5222–5230.
27 B. B. Wu, Y. Li, K. Su, L. Tan, X. M. Liu, Z. D. Cui, X. J. Yang, Y. Q. Liang, Z. Y. Li, S. L. Zhu, K. W. K. Yeung and S. L. Wu, *J. Hazard. Mater.*, 2019, **377**, 227–236.
28 T. Du, S. Y. Chen, J. Y. Zhang, T. T. Li, P. Li, J. F. Liu, X. J. Du and S. Wang, *Nanomaterials*, 2020, **10**, 1545.
29 N. Jiang, Y. L. Wang, K. C. Chan, C. Y. Chan, H. Z. Sun and G. J. Li, *Global Challenges*, 2020, **4**, 1900054.
30 X. M. Wang, L. Huang, Y. J. Wang, L. Xuan, W. W. Li and L. J. Tian, *Chem. Eng. J.*, 2021, **405**, 126711.
31 M. Ghidiu, M. R. Lukatskaya, M. Q. Zhao, Y. Gogotsi and M. W. Barsoum, *Nature*, 2014, **516**, 78–U171.
32 H. Lin, X. Wang, L. Yu, Y. Chen and J. Shi, *Nano Lett.*, 2017, **17**, 384–391.
33 M. Naguib, V. N. Mochalin, M. W. Barsoum and Y. Gogotsi, *Adv. Mater.*, 2014, **26**, 992–1005.
34 A. Maleki, J. He, S. Bochani, V. Nosrati, M.-A. Shahbazi and B. Guo, *ACS Nano*, 2021, **15**, 18895–18930.
35 F. Wu, H. L. Zheng, W. Z. Wang, Q. Wu, Q. Zhang, J. Y. Guo, B. Z. Pu, X. Y. Shi, J. B. Li, X. M. Chen and W. L. Hong, *Sci. China Mater.*, 2021, **64**, 748–758.
36 J. Wu, Q. Yang, Q. Li, H. Li and F. Li, *Anal. Chem.*, 2021, **93**, 4084–4091.
37 Y. Zhang, L. Chen, R. Sun, R. Lv, T. Du, Y. Li, X. Zhang, R. Sheng and Y. Qi, *ACS Biomater. Sci. Eng.*, 2022, **8**, 638–648.
38 L. Liu, C. Wang, Y. Li, L. Qiu, S. Zhou, P. Cui, P. Jiang, X. Ni, R. Liu, X. Du, J. Wang and J. Xia, *Biomater. Sci.*, 2021, **9**, 5965–5976.

39 D. Zhang, L. Huang, D.-W. Sun, H. Pu and Q. Wei, *Chem. Eng. J.*, 2023, **452**, 139078.
40 X. W. Huang and P. Y. Wu, *Adv. Funct. Mater.*, 2020, **30**, 1910048.
41 Y. Yao, Z. Li, Y. Han, L. Xie, X. Zhao and Z. Zhu, *Chem. Eng. J.*, 2023, **451**, 139029.
42 Y. Y. Xing, M. L. Chen, Y. K. Zhao, J. B. Xu and X. H. Hou, *Microchim. Acta*, 2022, **189**, 1–10.
43 S. Zhang, P. Huang, J. Wang, Z. Zhuang, Z. Zhang and W.-Q. Han, *J. Phys. Chem. Lett.*, 2020, **11**, 1247–1254.
44 M. X. Zhao, Y. Tao, W. Huang and Y. He, *Phys. Chem. Chem. Phys.*, 2018, **20**, 28644–28648.
45 S. Y. Feng, F. T. Wen, L. He, J. Y. Su, P. Jiang and D. P. He, *Sens. Actuators, B*, 2022, **361**, 131745.
46 J. Bonet-Aleta, J. I. Garcia-Peiro, S. Irusta and J. L. Hueso, *Nanomaterials*, 2022, **12**, 755.
47 Y. Yu, P. Li, C. Zhu, N. Ning, S. Zhang and G. J. Vancso, *Adv. Funct. Mater.*, 2019, **29**, 1904402.
48 A. Asati, C. Kaittanis, S. Santra and J. M. Perez, *Anal. Chem.*, 2011, **83**, 2547–2553.
49 X. L. Li, H. W. Chang, L. J. Zeng, X. R. Huang, Y. C. Li, R. F. Li and Z. J. Xi, *Energy Convers. Manage.*, 2020, **226**, 113515.
50 Z. Y. Wu, C. R. Li, Z. Li, K. Feng, M. J. Cai, D. K. Zhang, S. H. Wang, M. Y. Chu, C. C. Zhang, J. H. Shen, Z. Huang, Y. L. Xiao, G. A. Ozin, X. H. Zhang and L. He, *ACS Nano*, 2021, **15**, 5696–5705.
51 F. Shahzad, M. Alhabeb, C. B. Hatter, B. Anasori, S. Man Hong, C. M. Koo and Y. Gogotsi, *Science*, 2016, **353**, 1137–1140.
52 C. G. Wang, X. L. Cheng, H. Peng and Y. W. Zhang, *Nanoscale Res. Lett.*, 2022, **17**, 1–16.
53 Z. Liu, S. J. Zhang, H. Lin, M. L. Zhao, H. L. Yao, L. L. Zhang, W. J. Peng and Y. Chen, *Biomaterials*, 2018, **155**, 54–63.
54 K. Rasool, M. Helal, A. Ali, C. E. Ren, Y. Gogotsi and K. A. Mahmoud, *ACS Nano*, 2016, **10**, 3674–3684.
55 Y. Zhang, T. Zhao, X. Zhang, M. H. Akhtar, Q. Zhang, M. Li and C. Yu, *Sens. Actuators, B*, 2021, **346**, 130494.
56 W. Chen, Y. Y. Yan, R. L. Han, J. Hu, Y. F. Hou and K. Q. Tang, *Photochem. Photobiol. Sci.*, 2021, **20**, 153–160.